

Coupling between improper ferroelectricity and ferrimagnetism in the hexagonal ferrite LuFeO_3 Hena Das *

Laboratory for Materials and Structures, Tokyo Institute of Technology, 4259 Nagatsuta, Midori-ku, Yokohama, Kanagawa 226-8503, Japan; Tokyo Tech World Research Hub Initiative (WRHI), Institute of Innovative Research, Tokyo Institute of Technology, 4259 Nagatsuta, Midori-ku, Yokohama, Kanagawa 226-8503, Japan; and Kanagawa Institute of Industrial Science and Technology, 705-1 Shimo-Ogino, Ebina, Kanagawa 243-0435, Japan

 (Received 9 February 2022; revised 24 November 2022; accepted 29 November 2022; published 6 January 2023)

Here, we propose an idea to realize noncollinear ferrimagnetic orders with a considerably high magnetization \mathbf{M} and their coupling with an improper ferroelectric (FE) order in hexagonal LuFeO_3 type systems which exhibit interesting topological orders. These magnetic and magnetoelectric phenomena are driven by the antisymmetric Dzyaloshinskii-Moriya interactions between the magnetic ions and their coupling with the ferroelectricity. The proposed two-sublattice magnetic system, generated by a specific charge-ordered state, forms multiple energetically close, noncollinear ferrimagnetic orders. This offers a platform to manipulate the microscopic magnetic interactions and to trigger spin-reorientation (SR) transitions by various efficient means. The two-sublattice structure was realized in the hexagonal phase of LuFeO_3 doped with electrons. The proposed electron-doped systems are expected to exhibit switchable electric polarization ($P \sim 6\text{--}15 \mu\text{C}/\text{cm}^2$), considerably high magnetization ($M \sim 1.1\text{--}1.3 \mu_B/\text{Fe}$), and magnetic transition near room temperature ($\sim 275\text{--}290 \text{ K}$). Based on the coupling between the magnetic interactions and the FE primary order parameter observed in this system, microscopic mechanisms to achieve electric field \mathbf{E} induced SR transitions and 180° switching of the direction of \mathbf{M} are discussed.

DOI: [10.1103/PhysRevResearch.5.013007](https://doi.org/10.1103/PhysRevResearch.5.013007)

I. INTRODUCTION

The antisymmetric anisotropic Dzyaloshinskii-Moriya (DM) [1–3] exchange interaction between the localized spins in a magnetic material, which was proposed to comprehend the weak ferromagnetism [4], has been frequently found to play a vital role in driving coupling between the electric and magnetic degrees of freedom in magnetoelectric (ME) multiferroics [5–9]. However, this interaction being much weaker in comparison to its symmetric isotropic exchange counterpart, induces either weak ME effect or weak magnetization (\mathbf{M}) [4] in a single phase system, thereby impairing its device applicability [10,11]. For instance, in a LuFeO_3 type crystal lattice, a DM interaction induced, strong ME coupling was predicted [12]. LuFeO_3 exhibits an improper ferroelectric (FE) behavior with an electric polarization of $P \sim 6.5 \mu\text{C}/\text{cm}^2$ below $\sim 1040 \text{ K}$ driven by a zone boundary [$\mathbf{k} = (\frac{1}{3}, \frac{1}{3}, 0)$] structural distortion \mathbf{Q}_{K_3} , characterized by K_3 symmetry of the paraelectric (PE) $P6_3/mmc$ phase [13–15] and antiferromagnetic (AFM) order below $\sim 147 \text{ K}$ [16–19]. The nontrivial coupling between the DM interactions and \mathbf{Q}_{K_3} exhibits a potential to form ME domain structures

with topological defects and 180° switching of \mathbf{M} [12,20]. The induced magnetization ($M \sim 0.03 \mu_B/\text{Fe}$), however, is very weak [16–21]. In LuFe_2O_4 , a coupling between charge and magnetic order leads to the formation of collinear ferrimagnetic behavior [22–24] with considerably high $M \sim 0.8\text{--}1.4 \mu_B/\text{Fe}$ [25–28]. Here, a $\text{Fe}^{2+}/\text{Fe}^{3+}$ charge ordered (CO) pattern (C_q) characterized by the two-dimensional wave vector $\mathbf{q} = (\frac{1}{3}, \frac{1}{3})$ [25–28] creates two magnetic sublattices and the complex interactions between them drives the ferrimagnetic order. However, there exists ambiguity pertaining to its FE and ME coupling phenomena [21,25–27,29–32]. Here, we seek to explore the possible coupling between the charge and the magnetic orders in the LuFeO_3 crystal lattice, which exhibits strong coupling between the DM interactions and ferroelectricity.

Employing first-principles density functional theory (DFT) calculations and finite temperature Monte Carlo (MC) simulations, we show that the creation of two magnetic sublattices via a C_q type CO pattern and the cross-talk between them via the DM interactions can create intriguing phenomena such as noncollinear ferrimagnetic orders with considerably high magnetization \mathbf{M} , spin-reorientation (SR) transitions, and 180° ME switching, where \mathbf{P} and \mathbf{M} simultaneously switch their individual orientations. The two-sublattice system, where a Fe^{2+} triangular lattice is embedded within a Fe^{3+} hexagonal lattice, was created in the LuFeO_3 crystal lattice under electron doping. The doped system retains its improper FE nature with an electric polarization \mathbf{P} in par with the parent system forming various energetically close

*das.h.aa@m.titech.ac.jp

Published by the American Physical Society under the terms of the Creative Commons Attribution 4.0 International license. Further distribution of this work must maintain attribution to the author(s) and the published article's title, journal citation, and DOI.

noncollinear ferrimagnetic cooperative orders. The spins in the two magnetic sublattices are aligned in mutually perpendicular (\perp) directions due to the intersublattice DM interactions, generating an opportunity to achieve electric field (\mathbf{E}) induced SR transitions and ultrafast magnetization control [24,33–38]. Based on the interplay between the intersublattice DM interactions and \mathbf{Q}_{K_3} , we discussed the microscopic mechanisms to achieve \mathbf{E} induced SR transitions and 180° ME switching.

II. COMPUTATIONAL DETAILS

The first-principles calculations were conducted employing the density functional theory DFT + U method [39] with the Perdew-Burke-Ernzerhof form of the GGA (generalized-gradient approximation) exchange correlation functional [40] and using the projector augmented plane wave basis based method as implemented in the VASP (Vienna *Ab initio* Simulation Package) [41,42]. We considered $U = 4.5$ eV and $J_H = 0.95$ eV for the parent LuFeO₃ system as was used in the previous studies [12,21,43]. We cross-checked the stability of the polar Fe²⁺/Fe³⁺ charge ordered structures with respect to the nonpolar and the disordered phase by varying the value of the effective Hubbard parameters [$U_{\text{eff}}^{\text{Fe}^{2+}} = (U - J_H)_{\text{Fe}^{2+}}$ and $U_{\text{eff}}^{\text{Fe}^{3+}} = (U - J_H)_{\text{Fe}^{3+}}$] at the Fe $3d$ states. We considered Lu $4f$ states in the core. Considering the polar $P6_3cm$ and nonpolar $P\bar{3}c1$ phases, structural relaxations were performed for both the parent LuFeO₃ and the carrier-doped systems, employing 0.001 eV/Å convergence criteria of the Hellmann-Feynman forces. We used a $6 \times 6 \times 2$ Monkhorst-Pack Γ centered k -point mesh and a kinetic energy cut-off value of 500 eV. In the case of the $\sqrt{2} \times \sqrt{2} \times 1$ cell size of the $P6_3cm$ and $P\bar{3}c1$ structures, we employed a $3 \times 6 \times 3$ Monkhorst-Pack Γ centered k -point mesh. We calculated the electric polarization using the Berry phase method [44] as implemented in VASP. To determine the lowest energy path associated with the $+\mathbf{P} \rightarrow -\mathbf{P}$ switching process, we employed the “climbing image nudged elastic band (cNEB)” method [45]. This method involves construction and optimization of intermediate configurations to determine the minimum energy transition path between the initial and the final states. We constructed five to seven such intermediate configurations in between the initial and the final states.

To explore the effect of chemical substitution, we studied the properties of Lu_{2/3}R_{1/3}FeO₃ ($R = \text{Ce, Hf, Zr, Te, Sn}$) compositions. We constructed both Lu/ R cation ordered and disordered structures. To simulate the effect of cation disordering we generated the special quasirandom structures (SQS) [46] considering the hexagonal and the perovskite phases. To create the SQS structures, we employed the method of close reproduction of the perfectly random network for the first few shells around a given site as implemented in the alloy theoretic automated toolkit [47]. In various complex oxide systems this method has been successfully employed to simulate the effect of cation disordering [48–50].

In order to estimate the symmetric isotropic exchange (SE) interactions between the magnetic ions, we conducted total energy calculations of multiple collinear spin orders. Additionally, the values of single-ion-anisotropy (SIA) pa-

rameters were calculated considering total energy of various noncollinear spin structures in the presence of spin-orbit (L - S) coupling as implemented in VASP [51].

We performed classical MC simulations using Metropolis algorithms [52,53] and proper periodic boundary conditions as implemented in our group MC package to investigate the stability of the magnetic phase as a function of temperature and magnetic parameters. We calculated total energy $\xi(T)$ as a function of temperature (T) by considering N_{MC} number of MC steps for each temperature step and performing N_{Fe} spin flips. Here N_{Fe} represents the total number of Fe ions in the MC supercell structure. During each spin-flip process the direction of the selected spin gets randomly rotated with a uniform probability distribution of the associated unit spin vector over a unit sphere. The specific heat as a function of temperature was calculated employing

$$C_v(T) = \frac{\langle \xi(T)^2 \rangle - \langle \xi(T) \rangle^2}{k_B T^2}, \quad (1)$$

where the angular brackets denote thermal average. We also calculated the magnetization of the system as a function of temperature as

$$M_\rho = \left\langle \frac{1}{N_{\text{Fe}}} \sum_{i=1}^{N_{\text{Fe}}} g \mu_B S_\rho^i \right\rangle, \quad (2)$$

where $\rho = 1, 2, 3$ represents components of \mathbf{M} along the Cartesian axes $x, y,$ and $z,$ respectively. μ_B is the Bohr magneton and $g \approx 2$ denotes the gyromagnetic ratio.

III. RESULTS AND DISCUSSIONS

A. Improper ferroelectric order

\mathbf{P} being the secondary effect of a primary distortion, \mathbf{Q}_{K_3} , the FE order in LuFeO₃ is improper. \mathbf{Q}_{K_3} , which breaks the inversion symmetry of $P6_3/mmc$, assumes the form of FeO₅ bipyramids tilted towards (away) the \tilde{z}_c axis and results in one-up/two-down (one-down/two-up) buckling of the Lu ions [12]. \mathbf{Q}_{K_3} is defined by its magnitude Q_{K_3} and a phase factor $\Phi = \frac{n\pi}{3}$, representing the direction of the tilt of FeO₅ bipyramids. The nonlinear coupling between \mathbf{Q}_{K_3} and $\mathbf{Q}_{\Gamma_2^-}$ induces the electric polarization \mathbf{P} directed along the crystallographic \mathbf{c} (\hat{z}) axis, following the Landau free energy [12,15],

$$\mathcal{F} \sim P Q_{K_3}^3 \cos(3\Phi), \quad (3)$$

where n assumes six discrete values ($n = 1, 2, 3, 4, 5, 6$) due to Z_6 symmetry, where \mathbf{P} of the odd and even number structures are oriented in mutually opposite directions [54]. This leads to the formation of topologically protected FE and ME vortex domain structures in rare-earth manganites and ferrites [20,55–61]. Notably, $P\bar{3}c1$ also transforms as K_3 symmetry [62]. GGA + U results considering $U = 4.5$ eV and $J_H = 0.95$ eV at the Fe sites [12,21,43,63], show that LuFeO₃ crystallizes in the FE $P6_3cm$ phase with 24 meV/f.u. lower in energy compared to the $P\bar{3}c1$ structure. It exhibits $P \sim 14$ $\mu\text{C}/\text{cm}^2$ which agrees with the previous reports [12].

To simulate the effect of carrier doping, first we introduced excess carriers in the system by changing the number of valence electrons and by adding a homogeneous

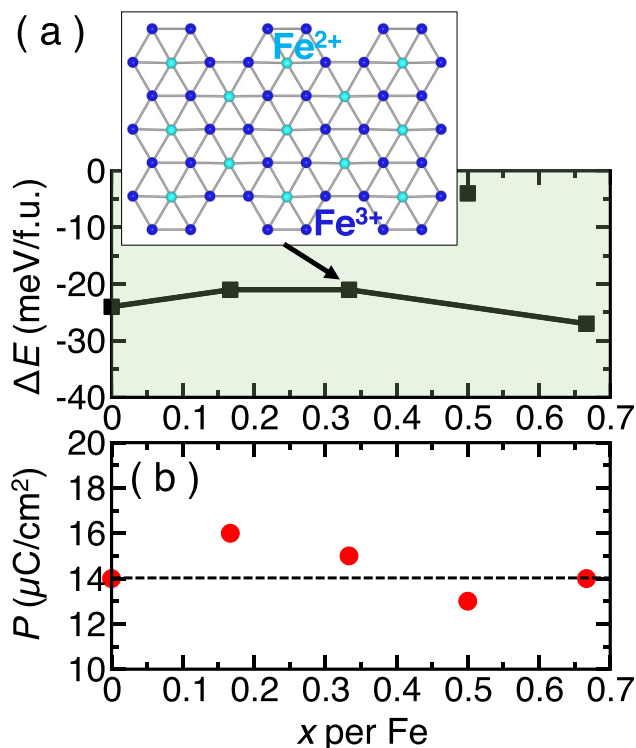


FIG. 1. (a) Relative stability (ΔE) of the polar phase with respect to the nonpolar phase as a function of electron doping concentrations x obtained by considering 12 formula unit cell size ($\sqrt{2} \times \sqrt{2} \times 1$ supercell of the polar $P6_3cm$ and nonpolar $P\bar{3}c1$ structures) for $U_{\text{eff}}^{\text{Fe}} = U - J_H = 3.55$ eV. Inset shows the C_q type $\text{Fe}^{2+}/\text{Fe}^{3+}$ charged ordered pattern, where the blue and cyan solid spheres represent the Fe^{3+} and Fe^{2+} ions, respectively. (b) Calculated values of the electric polarization as a function of the electron doping level x . The dashed line denotes the value of the electric polarization of the parent system.

background charge to keep it neutral, like in previous studies [64,65]. Optimizing both doped $P6_3cm$ and $P\bar{3}c1$ structures as a function of electron doping concentration x [see Fig. 1(a)], we observed that LuFeO_3 at the $x = \frac{1}{3}$ electrons (e^-) per Fe doping level shows the formation of two distinct types of Fe ions (Fig. 2). Here, $\frac{2}{3}$ of these ions show completely filled majority spin channels leaving the minority channels almost empty and hence a 3+ nominal oxidation state ($3d^5$ configuration), similar to LuFeO_3 [12,63]. The remaining $\frac{1}{3}$ Fe ions show partial occupancy in the minority spin channels (with the $3d^6$ electronic configuration resulting in a 2+ oxidation state) in addition to the completely filled majority spin channels. A C_q -type CO $Cmc2_1$ structure, with each Fe layer consisting of an Fe^{2+} triangular lattice embedded within the Fe^{3+} hexagonal lattice [Figs. 2(a) and 2(b)], as observed in LuFe_2O_4 [25, 66–69], is formed, independent of the effective Hubbard parameters at the Fe sites [62]. A similar cation ordered pattern was observed in $\text{InCu}_{2/3}\text{V}_{1/3}\text{O}_3$ [70,71]. The doped system exhibits \mathbf{Q}_{K_3} distortion characterized by an electric polarization $P \sim 15 \mu\text{C}/\text{cm}^2$ [see Fig. 1(b)] and insulating behavior with ~ 0.8 eV

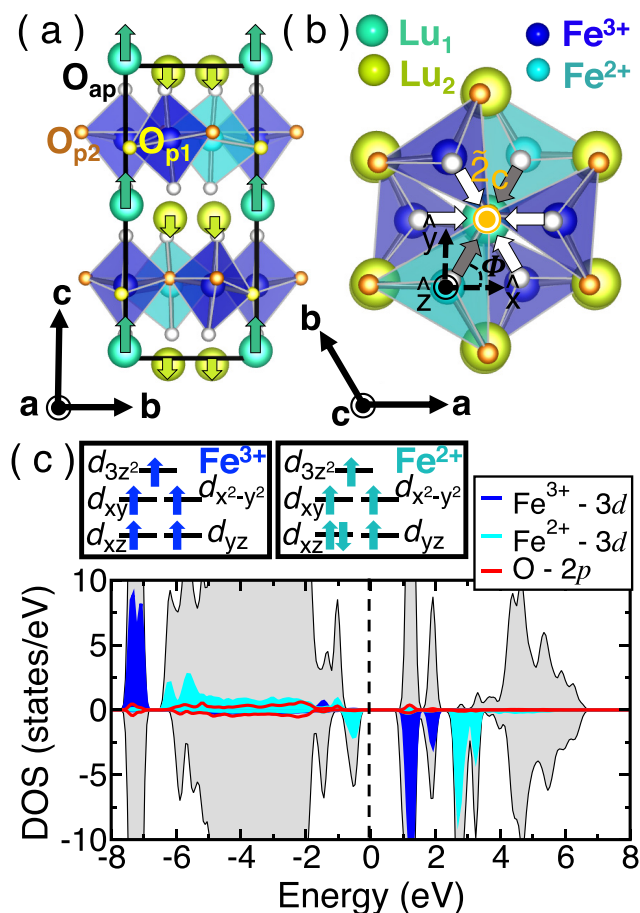


FIG. 2. $Cmc2_1$ crystal structure of the electron-doped LuFeO_3 exhibiting \mathbf{Q}_{K_3} distortion consists of (a) one-up/two-down buckling (denoted with arrows) of the Lu layer and (b) tilting of the FeO_5 trigonal bipyramids (represented by the arrows) towards the twofold screw axis \tilde{z}_c . The phase factor Φ is defined with respect to the Cartesian coordinate. (c) Upper panel: electron occupancy of the Fe^{3+} and Fe^{2+} ions. Lower panel: calculated density of states (DOS) of the electron-doped LuFeO_3 . Right panel: electron occupancy of the Fe^{3+} and Fe^{2+} ions. The trigonal bipyramid oxygen environment splits the $3d$ level of the Fe ions as e' (d_{xz} and d_{yz}), e'' (d_{xy} and $d_{x^2-y^2}$), and a'_1 (d_{3z^2}), in the order of increasing energy.

band gap, as in LuFeO_3 . We denote this structure as S-I.

Next, to determine the feasibility of the experimental realization of the proposed CO polar structures, we explored the chemical substitution route of electron doping. We studied the systems where Lu^{3+} ions are partially substituted by 4+ cations. We started our investigations with $\text{Lu}_{2/3}\text{Ce}_{1/3}\text{FeO}_3$ composition, where $\frac{1}{3}$ of the Lu ions were substituted by Ce ions, as the ionic radius of a tetravalent Ce ion is comparable to that of a trivalent Lu ion. Thereafter, we optimized the crystal structures of multiple Lu/Ce cation ordered configurations constructed from the $P6_3cm$, $P\bar{3}c1$, and $P6_3/mmc$ structures. The lowest energy structure had polar $P1$ symmetry, crystallized in the $P6_3cm$ type polar structure and exhibited considerable \mathbf{Q}_{K_3} type distortion. The Ce ions, irrespective of the Lu/Ce ordered pattern, were found to stabilize

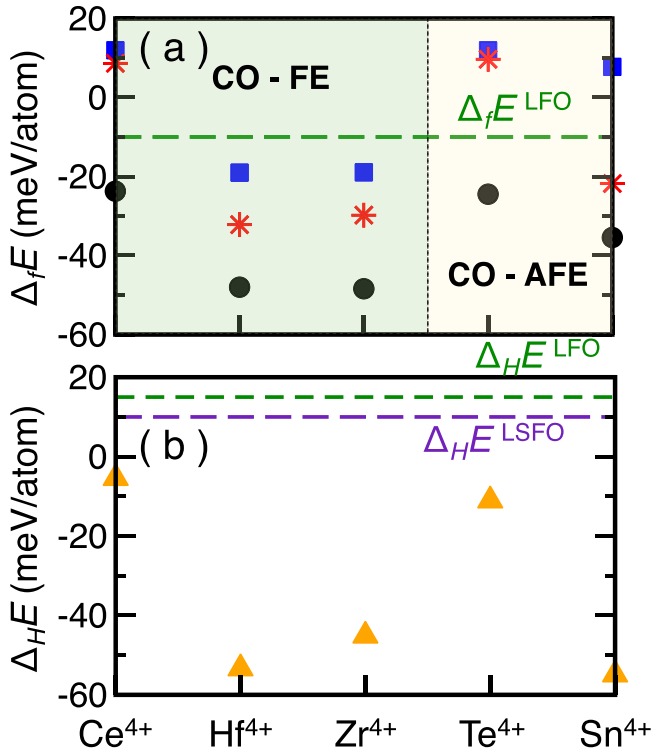


FIG. 3. (a) Formation energies ($\Delta_f E$) of the $\text{Lu}_{2/3}\text{R}_{1/3}\text{FeO}_3$ ($R = \text{Ce}, \text{Hf}, \text{Zr}, \text{Te}, \text{Sn}$) chemical compositions calculated by employing the formula given in Eq. (4). Formation energies of the lowest energy cation ordered structures exhibiting $\text{Fe}^{2+}/\text{Fe}^{3+}$ charge disproportionation (S_{CD}), cation ordered structures without $\text{Fe}^{2+}/\text{Fe}^{3+}$ charge disproportionation (S_{WCD}), and the SQS structures (S_{SQS}) are presented with solid black spheres, blue squares, and red stars, respectively. (b) Relative stability ($\Delta_H E$) of the hexagonal phases of $\text{Lu}_{2/3}\text{R}_{1/3}\text{FeO}_3$ compositions with respect to their perovskite counterparts. The calculated values of $\Delta_H E$ for LuFeO_3 (LFO) and $\text{Lu}_{2/3}\text{Sc}_{1/3}\text{FeO}_3$ (LSFO) are shown with dashed green and purple lines, respectively.

in the +4 nominal oxidation state with $\sim 0.04\mu_B$ magnetic moment (see Fig. S6 in the Supplemental Material [62]). The direct consequence of this effect was the introduction of an electron per Ce^{4+} ion in the Fe layer and the subsequent formation of the C_q type $\text{Fe}^{2+}/\text{Fe}^{3+}$ CO pattern [Fig. 1(a)]. In order to study the effect of Lu/Ce cation disordering, we also constructed a special quasirandom structure (SQS) [46,47]. As shown in Fig. 3(a), the SQS structure is higher in energy compared to the lowest energy cation ordered CO polar $P1$ phase. Nevertheless, a C_q type $\text{Fe}^{2+}/\text{Fe}^{3+}$ CO pattern and the polar atomic displacement pattern were found to form in the former structure. We further broadened our search considering other cations that tend to stabilize in tetravalent state. The results are summarized in Fig. 3. We observed that, similar to the S-I structure, Hf and Zr substituted systems stabilize in the polar C_q type $\text{Fe}^{2+}/\text{Fe}^{3+}$ CO phase with $Cmc2_1$ symmetry and exhibit insulating behavior. On the other hand, though the lowest energy Sn and Te substituted structures show the formation of a C_q type $\text{Fe}^{2+}/\text{Fe}^{3+}$ CO pattern, they get stabilized in the $P\bar{3}c1$ type antiferroelectric (AFE) phase. Notably, in the case of all the systems under the present study, the cation ordered structures forming $\text{Fe}^{2+}/\text{Fe}^{3+}$ charge disproportionation (CD)

and C_q type order (S_{CD}) are lower in energy compared to the SQS structures (S_{SQS}) and the structures which do not exhibit the $\text{Fe}^{2+}/\text{Fe}^{3+}$ CD phenomenon (S_{WCD}) [see Fig. 3(a)].

Figure 3(a) shows the formation energies of the $\text{Lu}_{2/3}\text{R}_{1/3}\text{FeO}_3$ ($R = \text{Ce}, \text{Hf}, \text{Zr}, \text{Sn}, \text{Te}$) compositions with respect to the energies associated with their decomposition into stable binary oxides as reported in the Materials Project [72] database. The corresponding formation energy is given by

$$\Delta_f E = E[\text{Lu}_{2/3}\text{R}_{1/3}\text{FeO}_3] - \frac{1}{3}E[\text{Lu}_2\text{O}_3] - \frac{1}{3}E[\text{RO}_2] - \frac{1}{3}E[\text{Fe}_2\text{O}_3] - \frac{1}{3}E[\text{FeO}]. \quad (4)$$

We optimized the structure of the binary oxides by initiating our calculations from the structures reported in the Materials Project [72] database. We observed that the tendency of formation of the hexagonal phase of $\text{Lu}_{2/3}\text{R}_{1/3}\text{FeO}_3$ compositions is higher compared to that of the hexagonal phase of the parent LuFeO_3 system [see Fig. 3(a), where $\Delta_f E^{\text{LFO}} = E[\text{LuFeO}_3] - \frac{1}{2}E[\text{Lu}_2\text{O}_3] - \frac{1}{2}E[\text{Fe}_2\text{O}_3]$]. Additionally, we also investigated the comparative likelihood of the Lu and the Fe sites to be occupied by the 4+ cations. We observed that the formation of the 4+ cations at the sixfold oxygen coordinated Lu sites is energetically most favorable (Fig. S5 in the Supplemental Material [62]). This is in agreement with the recent experimental observations on the Zr-doped $\text{Lu}_{0.5}\text{Sc}_{0.5}\text{FeO}_3$ [73] system. The formation of both Fe^{2+} and Fe^{3+} ions due to the substitution by the Zr^{4+} ions was also reported through x-ray photoelectron spectroscopy measurements.

The orthorhombic $Pnma$ structure of AFeO_3 systems ($A = \text{rare earth}, \text{Y}, \text{Sc}$) are reported to be more stable compared to their hexagonal counterpart. The hexagonal phase of LuFeO_3 was synthesized via a thin-film stabilization [74] method. Chemical substitution of Lu^{3+} ions with Sc^{3+} ions was found to be an effective route to stabilize the bulk hexagonal phase of LuFeO_3 [75,76]. We indeed observed an enhancement in the stability of the hexagonal phase compared to its perovskite counterpart in the Sc substituted system [Fig. 3(b)]. Interestingly, in the case of the 4+ cation substituted systems the hexagonal phase is lower in energy compared to the orthorhombic $Pnma$ structure [see Fig. 3(b)], indicating the feasibility of the formation of the hexagonal polar C_q type $\text{Fe}^{2+}/\text{Fe}^{3+}$ CO phase. This observation is consistent for both cation ordered and disordered structures. We refer to the 4+ cation substituted polar CO structures as S-II. A comparative analysis of the Fe-Fe connecting pathways of the parent, S-I and S-II structures, provided in Fig. S7 in the Supplemental Material [62], indicates that the S-II structures are expected to exhibit magnetic behavior similar to that of the S-I system.

In the case of LuFeO_3 type systems, as we have discussed before, the direction of \mathbf{P} is coupled with the direction of the \mathbf{Q}_{K_3} vector. Therefore, the change in the direction of \mathbf{P} by the application of electric field (\mathbf{E}) is expected to be associated with the change in the direction of the \mathbf{Q}_{K_3} vector. We note that a switchable electric polarization with the coercive field (E_c) of ~ 800 kV/cm at 300 K was observed in LuFeO_3 thin films [77]. Moreover, the formation of switchable electric polarization was also observed in various other

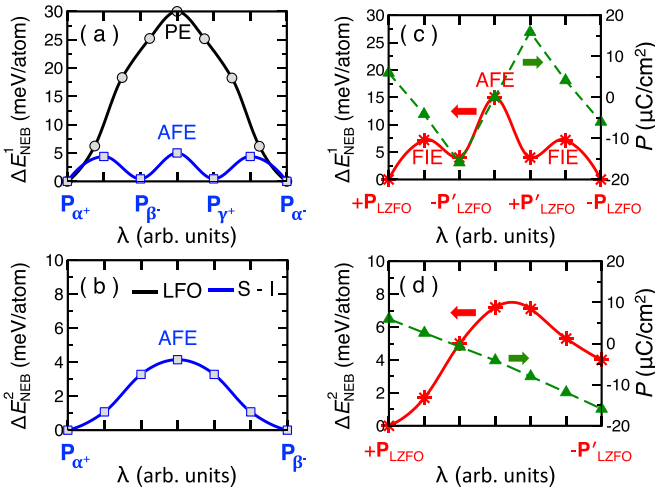


FIG. 4. The lowest energy switching paths associated with the $\mathbf{P}_{\alpha^+}(\Phi=0) \rightarrow \mathbf{P}_{\alpha^-}(\Phi=\pi)$ process of LuFeO₃ (LFO) and the S-I polar structures determined by the cNEB method. λ represents NEB steps in arbitrary units (arb. units). (b) Calculated energy as a function of λ corresponding to the $\mathbf{P}_{\alpha^+}(\Phi=0) \rightarrow \mathbf{P}_{\beta^-}(\Phi=\pi/3)$ switching pathway of the S-I structure. (c),(d) The lowest energy switching paths and the corresponding electric polarization associated with the $\mathbf{P}_{\text{LZFO}} \rightarrow -\mathbf{P}_{\text{LZFO}}$ and the $\mathbf{P}_{\text{LZFO}} \rightarrow -\mathbf{P}'_{\text{LZFO}}$ processes, respectively, for Lu_{2/3}Zr_{1/3}FeO₃ (LZFO) composition. The stars and the solid triangle represent the calculated energies and electric polarization as a function of λ , respectively.

AFeO₃ hexagonal systems [78–81]. We determined the electric polarization switching process ($\mathbf{P} \rightarrow -\mathbf{P}$) by employing the cNEB method [45] and calculated the associated energy barrier height. The $-\mathbf{P}$ state was constructed by inverting the pattern of the atomic displacements and by optimizing the structure thereafter. We refer to this process as $\mathbf{P}_{\alpha^+}(\Phi=0) \rightarrow \mathbf{P}_{\alpha^-}(\Phi=\pi)$ as it involves the 180° rotation of the \mathbf{Q}_{K_3} vector. The results corresponding to the parent and the S-I structures are shown in Fig. 4(a). We observed that in the case of the parent system, the trajectory is mediated by the PE $P6_3/mmc$ structure with an energy barrier of ~ 30 meV/atom. On the other hand, the electron-doped S-I structure shows a three-step $+\mathbf{P} \rightarrow -\mathbf{P}$ switching process mediating through the polar $\beta^-(\Phi = +\pi/3)$ and $\gamma^+(\Phi = +2\pi/3)$ type phases, as defined in the parent system [12]. The intermediate β^- and γ^+ phases are equivalent to the α^- and the α^+ phases, respectively. This indicates that the lowest energy $+\mathbf{P} \rightarrow -\mathbf{P}$ switching process is associated with $\pm\pi/3$ rotation of the \mathbf{Q}_{K_3} vector having energy barrier ~ 4 meV/atom [see Fig. 4(b)], which is lower in value than that of the parent system. Employing the same method, we also investigated the electric polarization switching phenomena of the chemically substituted systems. The results for Lu_{2/3}Zr_{1/3}FeO₃ (LZFO) are shown in Figs. 4(b) and 4(c). The calculated electric polarization of the most stable polar $Cmc2_1$ structure is $P_{\text{LZFO}} \sim 6 \mu\text{C}/\text{cm}^2$. Interestingly, similar to the S-I structure, our results show a three-step $+\mathbf{P}_{\text{LZFO}} \rightarrow -\mathbf{P}_{\text{LZFO}}$ switching process mediated via intermediate polar Cc structures having polarization $P'_{\text{LZFO}} \sim 16 \mu\text{C}/\text{cm}^2$ [see Fig. 4(b)]. The $-\mathbf{P}'_{\text{LZFO}}$ state has ~ 4 meV/atom higher energy than the $+\mathbf{P}_{\text{LZFO}}$ state. The $+\mathbf{P}_{\text{LZFO}} \rightarrow -\mathbf{P}'_{\text{LZFO}}$ asymmetric and the $-\mathbf{P}'_{\text{LZFO}} \rightarrow +\mathbf{P}'_{\text{LZFO}}$ symmetric potential profiles have

~ 5 and 11 meV/atom energy barriers, respectively. While the former process is mediated through a ferrielectric (FIE) Cc phase, the latter is mediated via the AFE $C2/c$ phase. Both Ce and Hf substituted systems exhibit switching phenomena similar to LZFO with lowest energy barrier heights ~ 5 and 7 meV/atom, respectively, associated with the switching between two unequal polarization states, similar to asymmetric oxide ferroelectrics [82,83]. This observed asymmetric energy profile is attributed to the Lu/R cation ordering. A cation disordered system, on the other hand, is expected to show a symmetric energy profile as observed in the S-I structure.

Our results indicate that the electron-doped polar insulating C_q type Fe²⁺/Fe³⁺ CO phases are expected to form through chemical substitution. Also, the energy barriers associated with the lowest energy polarization switching pathways for the electron-doped systems are lower than that of PbTiO₃ [84] and BiFeO₃ [85] ferroelectrics. Therefore, a switchable electric polarization in the predicted electron-doped candidates is expected to be experimentally realized.

B. Magnetic order and its coupling with FE order

Spin Hamiltonian. To determine the resulting magnetic order of the two-sublattice system, we conducted MC simulations considering spin Hamiltonian defined as

$$H = \sum_{i \neq j} J_{ij} \mathbf{S}_i \cdot \mathbf{S}_j + \sum_{i \neq j} \mathbf{D}_{ij} \cdot \mathbf{S}_i \times \mathbf{S}_j + \sum_i \mathbf{S}_i \cdot \hat{\tau}_i \cdot \mathbf{S}_i, \quad (5)$$

where J_{ij} and \mathbf{D}_{ij} represent the Fe-Fe symmetric isotropic exchange (SE) and DM interactions, respectively. $\hat{\tau}_i$ denotes the SIA tensor of the Fe ions. The spin Hamiltonian consists of nearest-neighbor (NN), second-nearest-neighbor (2NN) in-plane and effective interlayer Fe-Fe SE interactions and the corresponding energy term is given by

$$\begin{aligned} H_{SE} = & \sum_{\langle i_{\gamma_1}, j_{\gamma_1} \rangle_{NN}} J_{NN}^{[\gamma_1, \gamma_1]} \mathbf{S}_{i_{\gamma_1}}^{\gamma_1} \cdot \mathbf{S}_{j_{\gamma_1}}^{\gamma_1} \\ & + \sum_{\langle i_{\gamma_1}, j_{\gamma_1} \rangle_{2NN}} J_{2NN}^{[\gamma_1, \gamma_1]} \mathbf{S}_{i_{\gamma_1}}^{\gamma_1} \cdot \mathbf{S}_{j_{\gamma_1}}^{\gamma_1} + \sum_{\langle i_{\gamma_1}, j_{\gamma_1} \rangle_c} J_{c_{i_{\gamma_1} j_{\gamma_1}}}^{[\gamma_1, \gamma_1]} \mathbf{S}_{i_{\gamma_1}}^{\gamma_1} \cdot \mathbf{S}_{j_{\gamma_1}}^{\gamma_1} \\ & + \sum_{\langle i_{\gamma_2}, j_{\gamma_2} \rangle_{NN}} J_{NN}^{[\gamma_2, \gamma_2]} \mathbf{S}_{i_{\gamma_2}}^{\gamma_2} \cdot \mathbf{S}_{j_{\gamma_2}}^{\gamma_2} + \sum_{\langle i_{\gamma_2}, j_{\gamma_2} \rangle_c} J_{c_{i_{\gamma_2} j_{\gamma_2}}}^{[\gamma_2, \gamma_2]} \mathbf{S}_{i_{\gamma_2}}^{\gamma_2} \cdot \mathbf{S}_{j_{\gamma_2}}^{\gamma_2} \\ & + \sum_{\langle i_{\gamma_2}, j_{\gamma_2} \rangle_{2NN}} J_{2NN}^{[\gamma_2, \gamma_2]} \mathbf{S}_{i_{\gamma_2}}^{\gamma_2} \cdot \mathbf{S}_{j_{\gamma_2}}^{\gamma_2} + \sum_{\langle i_{\gamma_2}, j_{\gamma_2} \rangle_c} J_{c_{i_{\gamma_2} j_{\gamma_2}}}^{[\gamma_2, \gamma_2]} \mathbf{S}_{i_{\gamma_2}}^{\gamma_2} \cdot \mathbf{S}_{j_{\gamma_2}}^{\gamma_2}, \end{aligned} \quad (6)$$

where γ_1 and γ_2 represent two magnetic sublattices as illustrated in Fig. 5(a). Here $(i_{\gamma_1}, j_{\gamma_1})$ and $(i_{\gamma_2}, j_{\gamma_2})$ denote the site of the Fe ^{γ_1} (S^{γ_1}) and Fe ^{γ_2} (S^{γ_2}) spins in the γ_1 and γ_2 sublattices, respectively. The SE interactions between the consecutive Fe layers mediated via Fe-O-Lu-O-Fe pathways along the crystallographic c axis ($J_{c_{i_{\gamma_1} j_{\gamma_1}}}^{[\gamma_1, \gamma_1]}$, $J_{c_{i_{\gamma_2} j_{\gamma_2}}}^{[\gamma_2, \gamma_2]}$, $J_{c_{i_{\gamma_2} j_{\gamma_1}}}^{[\gamma_2, \gamma_1]}$) were taken into account.

NN Fe-Fe DM interactions are depicted in Fig. 5(b), where the transverse components are induced by \mathbf{Q}_{K_3} and the longitudinal components are already existing in the PE phase. The DM vectors in the consecutive Fe layers are antiparallel to each other due to $\hat{2}_c$ symmetry. The corresponding energy

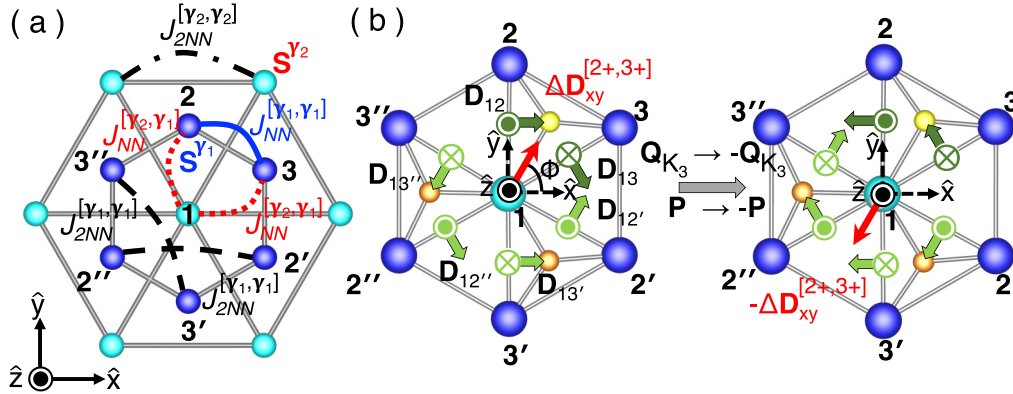


FIG. 5. (a) Symmetric isotropic in-plane exchange interactions between Fe spins in a two-sublattice (γ_1 and γ_2) model. We considered inter- ($J_{NN}^{[\gamma_2, \gamma_1]}$) and intra- ($J_{NN}^{[\gamma_1, \gamma_1]}$) sublattice NN symmetric isotropic exchange (SE) interactions. Also, the intrasublattice 2NN SE interactions ($J_{2NN}^{[\gamma_1, \gamma_1]}$ and $J_{2NN}^{[\gamma_2, \gamma_2]}$) were taken into account. The sites occupied by the S^{γ_1} and S^{γ_2} spins are represented by the blue and cyan solid spheres, respectively. (b) NN DM vectors acting on the Fe 1 of a single Fe layer. The longitudinal components of the DM vectors orientated along the positive and negative \hat{z} directions are shown with dots and cross marks, respectively. The \mathbf{Q}_{K_3} distortions induce two nonequivalent transverse components of DM vectors mediated through planar oxygens O_{p1} ($D_{12} = D_{13} = D$) and O_{p2} ($D_{12'} = D_{13'} = D_{12''} = D_{13''} = D'$), respectively. $\Delta D_{xy}^{[2+,3+]}$ denotes effective DM interaction acting on Fe 1 as derived in Eq. (11). The transverse components switch their direction with the $\mathbf{Q}_{K_3} \rightarrow -\mathbf{Q}_{K_3}$ ($\mathbf{P} \rightarrow -\mathbf{P}$) switching process.

contribution is given by

$$H_{DM} = \sum_{(i_{\gamma_1}, j_{\gamma_1})_{NN}} \mathbf{D}_{NN}^{[\gamma_1, \gamma_1]} \cdot \mathbf{S}_{i_{\gamma_1}}^{\gamma_1} \times \mathbf{S}_{j_{\gamma_1}}^{\gamma_1} + \sum_{(i_{\gamma_2}, j_{\gamma_1})_{NN}} \mathbf{D}_{NN}^{[\gamma_2, \gamma_1]} \cdot \mathbf{S}_{i_{\gamma_2}}^{\gamma_2} \times \mathbf{S}_{j_{\gamma_1}}^{\gamma_1}, \quad (7)$$

where $\mathbf{D}_{NN}^{[\gamma_1, \gamma_1]}$ and $\mathbf{D}_{NN}^{[\gamma_2, \gamma_1]}$ denote NN intra- and intersublattice DM interactions between the Fe spins, respectively.

The energy contribution arising out of the magnetic anisotropy of the Fe ions is defined as

$$H_{SIA} = \sum_{i_{\gamma_1}} \mathbf{S}_{i_{\gamma_1}}^{\gamma_1} \cdot \hat{\tau}_{i_{\gamma_1}}^{\gamma_1} \cdot \mathbf{S}_{i_{\gamma_1}}^{\gamma_1} + \sum_{i_{\gamma_2}} \mathbf{S}_{i_{\gamma_2}}^{\gamma_2} \cdot \hat{\tau}_{i_{\gamma_2}}^{\gamma_2} \cdot \mathbf{S}_{i_{\gamma_2}}^{\gamma_2}, \quad (8)$$

where $\hat{\tau}^{\gamma_1}$ and $\hat{\tau}^{\gamma_2}$ denote the SIA tensors corresponding to the magnetic ions in the γ_1 and γ_2 sublattices, respectively.

Parent LuFeO₃ system. Figure 6(a) shows the results of MC simulations for LuFeO₃, where both the magnetic sublattices are occupied by the Fe³⁺ ions ($S^{3+} = \frac{5}{2}$), as functions of the transverse DM interactions between the Fe³⁺ spins ($D_{xy}^{[3+,3+]}$) and their SIA (τ^{3+}). An independent SIA parameter (τ^{3+}) which determines the tendency of the Fe spins to be oriented in the xy plane or along the \hat{z} axis was considered. The details of the spin model and MC simulations are given in the Supplemental Material [62]. The positive and the negative values of τ^{3+} indicate uniaxial (\hat{z}) and uniplanar (xy) magnetic anisotropy, respectively. In this system, both NN and 2NN SE interactions are AFM in nature with the estimated strengths of $J_{NN}^{[3+,3+]} \sim 6.3$ meV and $J_{2NN}^{[3+,3+]} \sim 0.3$ meV, respectively, agreeing well with the previous reports [12]. Geometric frustration created by the six NN AFM SE interactions in the triangular lattice induces the formation of multiple, energetically degenerate, 120° noncollinear orders [12]. The effective interlayer AFM $\Delta J_c^{[3+,3+]} = J_c - J'_c \sim 0.4$ meV interaction breaks the geometric frustration and stabilizes the A2 type magnetic order ($P6_3c'm'$) [Fig. 6(a)]. Here, J_c and J'_c represent

two nonequivalent SE interactions mediated through Fe-O-Lu-O-Fe pathways (see the Supplemental Material [62]). Notably, Fe³⁺ ions result in uniaxial (\hat{z}) magnetic anisotropy with $\tau^{3+} \sim 0.03$ meV, contrasting the in-plane (xy) magnetic anisotropy of Mn³⁺ ions in its manganite counterpart [12]. While in-plane magnetic anisotropy orders the spins in the A2 pattern on the xy plane, the uniaxial magnetic anisotropy causes a tilt in the A2 ordered plane [Fig. 6(a)]. The $D_{xy}^{[3+,3+]}$ generates a canted magnetization. DFT estimated values of magnetic parameters (see Tables S1 and S2 in the Supplemental Material [62]) stabilize $\theta \sim 45^\circ$ tilted A2 phase below ~ 148 K exhibiting a canted magnetization of $\sim 0.03 \mu_B/\text{Fe}$ [62]. These observations, on par with experimental reports [16–19], establish the effectiveness of the determined spin model.

Electron-doped system. Figure 6(b) shows the results of MC simulations for the two-sublattice system S-I. In this system, (1) the strength of the NN Fe³⁺ – Fe³⁺ SE interaction $J_{NN}^{[3+,3+]}$ is increased from 6.3 to 8.5 meV (primarily due to the enhancement of the $\angle \text{Fe}^{3+}\text{-O-Fe}^{3+}$ of the mediating path [62]), (2) the NN Fe²⁺ – Fe³⁺ SE interaction $J_{NN}^{[2+,3+]}$ ~ 1.1 meV is AFM in nature, and (3) while the 2NN Fe²⁺ – Fe²⁺ SE interaction $J_{2NN}^{[2+,2+]}$ ~ -0.1 meV is ferromagnetic (FM) in nature, the $J_{2NN}^{[3+,3+]}$ remains AFM in nature with a value of ~ 0.3 meV. An effective interlayer SE interaction, with a value identical to the same interaction in LuFeO₃, was considered [62]. We observed that the Fe²⁺ ions exhibit orbital moment $\mu_o^{2+} \sim 0.2 \mu_B$, which is an order of magnitude stronger than that of the Fe³⁺ ions ($\frac{\mu_o^{3+}}{\mu_o^{2+}} \sim 0.1$). The Fe²⁺ ions also exhibit uniaxial magnetic anisotropy having $\tau^{2+} \sim 0.2$ meV ($\frac{\tau^{3+}}{\tau^{2+}} \sim 0.1$). On the other hand, we employed the intersublattice DM interactions ($\mathbf{D}^{[2+,3+]}$) as a variable in MC simulations, which played a vital role in the determination of the magnetic order.

Our results [Fig. 6(b)] show the formation of noncollinear ferrimagnetic orders, where the FM ordered Fe²⁺ spins are

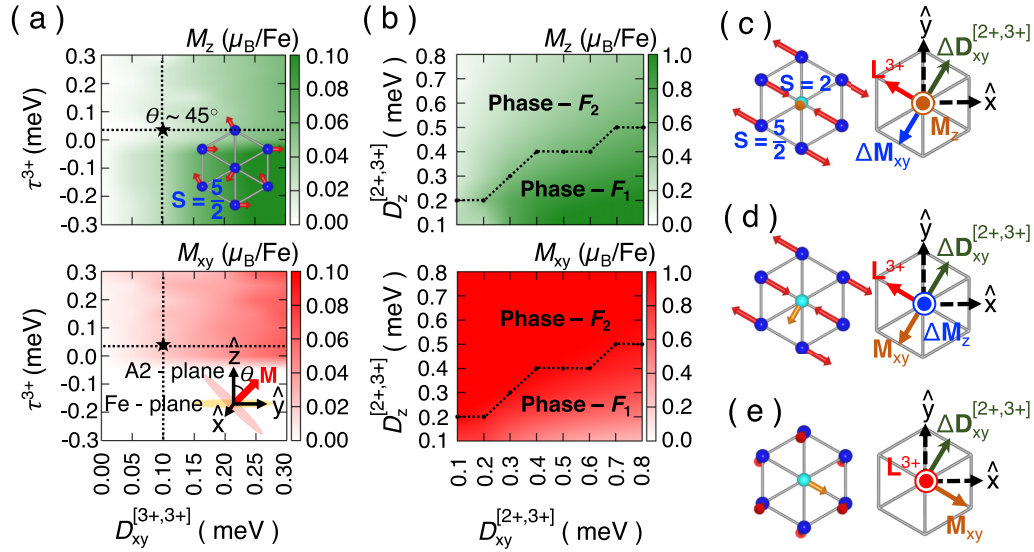


FIG. 6. (a) Calculated out-of-plane M_z (upper panel) and in-plane M_{xy} (lower panel) components of magnetization (\mathbf{M}) as functions of $D_{xy}^{[3+,3+]}$ and SIA parameter τ^{3+} for the parent system. Insets: A2 spin ordering and the tilt (θ) of the A2 spin ordered plane, which is denoted by the tilt of the direction of \mathbf{M} with respect to the \hat{z} axis. Star denotes DFT estimated values of $D_{xy}^{[3+,3+]}$ and τ^{3+} . The results correspond to $D_z^{[3+,3+]} \sim 0.1$ meV as estimated from DFT [12]. (b) Calculated out-of-plane M_z (upper panel) and in-plane M_{xy} (lower panel) magnetizations as functions of $D^{[2+,3+]}$ parameters for the system doped with $x = \frac{1}{3}$ per Fe e^- . (c)–(e) Identified noncollinear ferrimagnetic orders F_1 , F_2 , and F_3 , respectively, and their schematic representations. Red and orange arrows represent Fe^{3+} and Fe^{2+} spins, respectively.

perpendicularly oriented to the direction of the AFM ordered Fe^{3+} spins (\mathbf{L}^{3+} denotes AFM order parameter), resulting in a net magnetization \mathbf{M} . Without $D^{[2+,3+]}$, the Fe^{2+} spins do not show any cooperative order. Three magnetic phases were identified, namely, F_1 , F_2 , and F_3 [Figs. 6(c)–6(e)]. F_1 aligns the major components of the Fe^{2+} and Fe^{3+} spins along the \hat{z} axis and in the xy plane, respectively, giving rise to the longitudinal and transverse components of \mathbf{M} as

$$\mathbf{M}_z \propto \Delta \mathbf{D}_{xy}^{[2+,3+]} \times \mathbf{L}^{3+}, \quad (9)$$

$$\Delta \mathbf{M}_{xy} \propto \Delta \mathbf{D}_z^{[2+,3+]} \times \mathbf{L}^{3+}. \quad (10)$$

F_2 corresponds to coplanar, mutually perpendicular Fe^{2+} and Fe^{3+} spins with major \mathbf{M}_{xy} and minor $\Delta \mathbf{M}_z$ (induced by $\Delta \mathbf{D}_{xy}^{[2+,3+]}$) components. In F_3 , the major Fe^{2+} and Fe^{3+} spins are oriented in the xy plane and along the \hat{z} axis, respectively. The stability of these phases is controlled by the complex interplay between the effective $Fe^{2+} - Fe^{3+}$ DM interactions,

$$\Delta \mathbf{D}^{[2+,3+]} \approx (\bar{D}_{xy}^{[2+,3+]} \cos \Phi, \bar{D}_{xy}^{[2+,3+]} \sin \Phi, \bar{D}_z^{[2+,3+]}) \quad (11)$$

and the SIA (τ^{2+} and τ^{3+}). Here, $\bar{D}_{xy}^{[2+,3+]} = 2D_{xy}^{[2+,3+]}$ and $\bar{D}_z^{[2+,3+]} = 6D_z^{[2+,3+]}$. Both the direction and magnitude of $\bar{D}_{xy}^{[2+,3+]}$ are synchronized with \mathbf{Q}_{K_3} [Fig. 5(b)] [62].

Next, we conducted GGA + U total energy calculations considering the polar and nonpolar structures of the ferrimagnetic orders. The F_1 and the F_2 ground-state magnetic orders appear in the polar and the nonpolar phases, respectively [Fig. 7(a)]. These results are in harmony with the MC solutions obtained in the $D_{xy}^{[2+,3+]} > D_z^{[2+,3+]}$ magnetic parameter space [Fig. 7(b)]. This indicates an $F_1 \rightarrow F_2$ SR transition with the modulation of the $\Delta \mathbf{D}_{xy}^{[2+,3+]}$ parameter synchronized with \mathbf{Q}_{K_3} (Fig. 5). Temperature also drives an $F_1 \rightarrow F_3$

SR transition [Fig. 7(b)]. At low temperatures (~ 5 , K) F_1 cooperative order forms as $\frac{\tau^{2+}}{\tau^{3+}} > \frac{2(S^{3+})^2}{(S^{2+})^2}$. However, at high temperatures F_3 order is formed due to entropy. The paramagnetic (PM) to ferrimagnetic phase transition temperature (T_c) is primarily determined by the relative $\frac{J_{NN}^{[2+,3+]}}{J_{NN}^{[3+,3+]}}$ strength, which also controls the magnitude of magnetization [62]. In the e^- -doped system, $T_c \sim 290$ K and $M \sim 1.1 \mu_B/\text{Fe}$ (Fig. S18 in the Supplemental Material [62]), both are significantly higher than their LuFeO_3 counterparts [12,16–19], indicating an effective route to enhance the magnetic properties of LuFeO_3 . In fact, the C_4 type CO pattern was found to form at lower levels of doping with a potential to induce considerable enhancement in the magnetic properties of LuFeO_3 (Fig. S20 in the Supplemental Material [62]). Additionally, we also estimated the values of the magnetic parameters corresponding to the S-II structures (Tables S1 and S2 in the Supplemental Material [62]) and conducted the MC simulations. We observed that the magnetic behavior of the S-II systems are remarkably similar to that of the S-I system [see Figs. 7(c) and 7(d)], both exhibiting temperature induced $F_1 \rightarrow F_3$ transition. This has also been indicated by the comparable features in the Fe-Fe connecting pathways of these systems. The $\text{Lu}_{2/3}\text{R}_{1/3}\text{FeO}_3$ systems exhibit T_c and M ranging from 275 to 285 K and $M \sim 1.1$ to 1.3 μ_B/Fe , respectively. The $F_1 \rightarrow F_3$ SR transition takes place around 35 K. We cross-checked the MC predicted ground states by performing DFT + U calculations with L - S coupling.

Coupling between FE and magnetic order. As we have discussed before, in the case of the electron-doped systems, the $\mathbf{P} \rightarrow -\mathbf{P}$ process leads to the rotation of \mathbf{Q}_{K_3} by an angle $\Delta \Phi = \frac{\pi}{3}$. Here, we discuss probable ME processes based on the S-I structure. The trilinear coupling between $\Delta \mathbf{D}^{[2+,3+]}$,

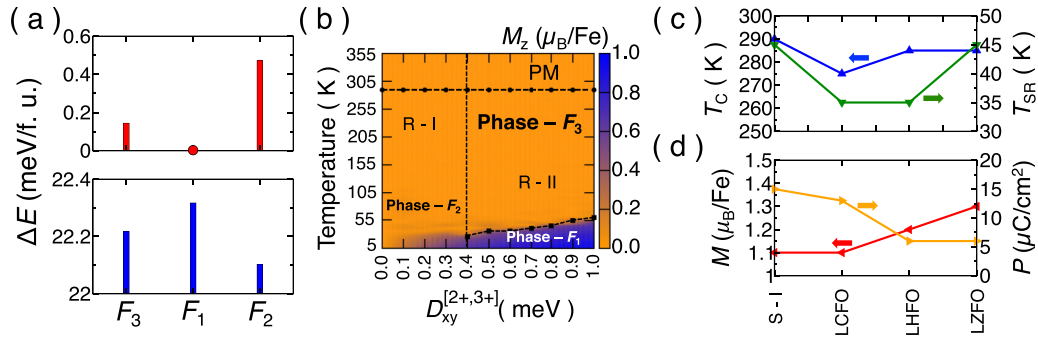


FIG. 7. (a) GGA + U calculated total energy of the ferrimagnetic phases in polar (upper panel) and nonpolar (lower panel) structures with respect to the energy of the polar F_1 phase. (b) Constructed temperature vs $D_{xy}^{[2+,3+]}$ phase diagram using MC results. PM represents paramagnetic phase. The PM to ferrimagnetic order and SR transition temperatures are marked with solid black spheres and squares, respectively. The parameter spaces R-I and R-II represent $|D_{xy}^{[2+,3+]}| < |D_z^{[2+,3+]}|$ and $|D_{xy}^{[2+,3+]}| > |D_z^{[2+,3+]}|$, respectively. (c) Estimated PM to ferrimagnetic F_3 and $F_3 \rightarrow F_1$ transition temperatures for the electron-doped systems by MC simulations. (d) Calculated magnetization M and polarization P of the electron-doped systems. LCFO, LHFO and LZFO denote $\text{Lu}_{2/3}\text{Ce}_{1/3}\text{FeO}_3$, $\text{Lu}_{2/3}\text{Hf}_{1/3}\text{FeO}_3$ and $\text{Lu}_{2/3}\text{Zr}_{1/3}\text{FeO}_3$ compositions, respectively.

\mathbf{M} , and \mathbf{L}^{3+} [Eqs. (9) and (10)] and the coupling between $\Delta\mathbf{D}^{[2+,3+]}$ and \mathbf{Q}_{K_3} [Eqs. (11) and Fig. 5] show that the rotation of the \mathbf{Q}_{K_3} vector induces either \mathbf{L}^{3+} or \mathbf{M}_z to rotate, thereby suggesting two probable ME processes [62]. The former process is characterized by the rotation of \mathbf{Q}_{K_3} by $\pm\frac{\pi}{3}$ leading both \mathbf{L}^{3+} and $\Delta\mathbf{M}_{xy}$ to rotate in phase by $\frac{\pi}{3}$. However, here, \mathbf{M}_z does not change its direction. In the latter case, the rotation of \mathbf{Q}_{K_3} by $\pm\frac{\pi}{3}$ induces both \mathbf{L}^{3+} and $\Delta\mathbf{M}_{xy}$ to rotate out of phase by $\frac{2\pi}{3}$ leading to the 180° switching of \mathbf{M}_z . In the present system, the $\mathbf{M}_z \rightarrow -\mathbf{M}_z$ process is expected to be more feasible, as the intermediate F_2 state exhibits the lowest transition barrier height [Figs. 7(a) and 7(b)] and is associated with lower magnetostatic energy. The S-II structures are expected to behave in a similar fashion.

IV. CONCLUSIONS

In summary, we predict noncollinear ferrimagnetism, SR transitions, and 180° ME switching phenomena governed by the coupling between charge ordering, DM interactions, and improper ferroelectricity. These predictions are based on MC simulations on a two-sublattice model, constructed by

doping the improper FE hexagonal phase of LuFeO_3 with electrons. We elucidate the prospective microscopic mechanisms to control the stabilization of ferrimagnetic orders by applying electric field \mathbf{E} induced SR transitions and 180° switching of \mathbf{M} . Our proposed model will expectedly contribute to a deeper understanding of the observed ME behavior of $(\text{LuFeO}_3)_m/(\text{LuFe}_2\text{O}_4)$ superlattices at room temperature [21,43,61], where formation of the e^- -doped head-to-head LuFeO_3 domain wall was reported. Our predictions are expected to motivate the designing of noncollinear ferrimagnetic materials with prospective applications in spintronics technology.

ACKNOWLEDGMENTS

H.D. acknowledges the fruitful discussions with S. Ghosh, M. J. Swamynadhan, A. O'Hara, and S. T. Pantelides. We also acknowledge the insightful discussions with J. Nordlander, M. E. Holtz, and J. A. Mundy. Research at the Tokyo Institute of Technology is supported by the Grants-in-Aid for Scientific Research Grants No. JP19K05246 and No. JP19H05625 from the Japan Society for the Promotion of Science (JSPS). H.D. also acknowledges computational support from TSUBAME supercomputing facility.

- [1] I. Dzyaloshinsky, A thermodynamic theory of weak ferromagnetism of antiferromagnetics, *J. Phys. Chem. Solids* **4**, 241 (1958).
- [2] T. Moriya, New Mechanism of Anisotropic Superexchange Interaction, *Phys. Rev. Lett.* **4**, 228 (1960).
- [3] T. Moriya, Anisotropic Superexchange Interaction and Weak Ferromagnetism, *Phys. Rev.* **120**, 91 (1960).
- [4] V. E. Dmitrienko, E. N. Ovchinnikova, S. P. Collins, G. Nisbet, G. Beutier, Y. O. Kvashnin, V. V. Mazurenko, A. I. Lichtenstein and M. I. Katsnelson, Measuring the Dzyaloshinskii-Moriya interaction in a weak ferromagnet, *Nat. Phys.* **10**, 202 (2014).
- [5] D. Khomskii, Classifying multiferroics: Mechanisms and effects, *Physics* **2**, 20 (2009).
- [6] W. Eerenstein, N. D. Mathur, and J. F. Scott, Multiferroic and magnetoelectric materials, *Nature (London)* **442**, 759 (2006).
- [7] S.-W. Cheong and M. Mostovoy, Multiferroics: A magnetic twist for ferroelectricity, *Nat. Mater.* **6**, 13 (2007).
- [8] M. Fiebig, T. Lottermoser, D. Meier, and M. Trassin, The evolution of multiferroics, *Nat. Rev. Mater.* **1**, 16046 (2016).
- [9] N. A. Spaldin and R. Ramesh, Advances in magnetoelectric multiferroics, *Nat. Mater.* **18**, 203 (2019).

- [10] F. Matsukura, Y. Tokura, and H. Ohno, Control of magnetism by electric fields, *Nat. Nanotechnol.* **10**, 209 (2015).
- [11] J. M. Hu and C. W. Nan, Opportunities and challenges for magnetoelectric devices, *APL Mater.* **7**, 080905 (2019).
- [12] H. Das, A. L. Wysocki, Y. Geng, W. Wu, and C. J. Fennie, Bulk magnetoelectricity in the hexagonal manganites and ferrites, *Nat. Commun.* **5**, 2998 (2014).
- [13] B. B. Van Aken, T. T. M. Palstra, A. Filippetti, and N. A. Spaldin, The origin of ferroelectricity in magnetoelectric YMnO_3 , *Nat. Mater.* **3**, 164 (2004).
- [14] C. J. Fennie and K. M. Rabe, Ferroelectric transition in YMnO_3 from first principles, *Phys. Rev. B* **72**, 100103(R) (2005).
- [15] S. Artyukhin, K. T. Delaney, N. A. Spaldin, and M. Mostovoy, Landau theory of topological defects in multiferroic hexagonal manganites, *Nat. Mater.* **13**, 42 (2014).
- [16] E. Magome, C. Moriyoshi, Y. Kuroiwa, A. Masuno, and H. Inoue, Noncentrosymmetric structure of LuFeO_3 in metastable state, *Jpn. J. Appl. Phys.* **49**, 09ME06 (2010).
- [17] W. Wang, J. Zhao, W. Wang, Z. Gai, N. Balke, M. Chi, H. N. Lee, W. Tian, L. Zhu, X. Cheng *et al.*, Room-Temperature Multiferroic Hexagonal LuFeO_3 Films, *Phys. Rev. Lett.* **110**, 237601 (2013).
- [18] S. M. Disseler, J. A. Borchers, C. M. Brooks, J. A. Mundy, J. A. Moyer, D. A. Hillsberry, E. L. Thies, D. A. Tenne, J. Heron, M. E. Holtz *et al.*, Magnetic Structure and Ordering of Multiferroic Hexagonal LuFeO_3 , *Phys. Rev. Lett.* **114**, 217602 (2015).
- [19] J. A. Moyer, R. Misra, J. A. Mundy, C. M. Brooks, J. T. Heron, D. A. Muller, D. G. Schlom, and P. Schiffer, Intrinsic magnetic properties of hexagonal LuFeO_3 and the effects of nonstoichiometry, *APL Mater.* **2**, 012106 (2014).
- [20] Y. Geng, H. Das, A. L. Wysocki, X. Wang, S.-W. Cheong, M. Mostovoy, C. J. Fennie, and W. Wu, Direct visualization of magnetoelectric domains, *Nat. Mater.* **13**, 163 (2014).
- [21] J. A. Mundy, C. M. Brooks, M. E. Holtz, J. A. Moyer, H. Das, A. F. Rébola, J. T. Heron, J. D. Clarkson, S. M. Disseler, Z. Liu *et al.*, Atomically engineered ferroic layers yield a room-temperature magnetoelectric multiferroic, *Nature (London)* **537**, 523 (2016).
- [22] L. Néel, Antiferromagnetism and Ferrimagnetism, *Proc. Phys. Soc. A* **65**, 869 (1952).
- [23] E. W. Gorter, Ionic distribution deduced from the g-factor of a ferrimagnetic spinel: Ti^{4+} in fourfold co-ordination, *Nature (London)* **173**, 123 (1954).
- [24] S. K. Kim, G. S. D. Beach, K.-J. Lee, T. Ono, T. Rasing, and H. Yang, Ferrimagnetic spintronics, *Nat. Mater.* **21**, 24 (2022).
- [25] N. Ikeda, H. Ohsumi, K. Ohwada, K. Ishii, T. Inami, K. Kakurai, Y. Murakami, K. Yoshii, S. Mori, Y. Horibe, and H. Kitô, Ferroelectricity from iron valence ordering in the charge-frustrated system LuFe_2O_4 , *Nature (London)* **436**, 1136 (2005).
- [26] A. D. Christianson, M. D. Lumsden, M. Angst, Z. Yamani, W. Tian, R. Jin, E. A. Payzant, S. E. Nagler, B. C. Sales, and D. Mandrus, Three-Dimensional Magnetic Correlations in Multiferroic LuFe_2O_4 , *Phys. Rev. Lett.* **100**, 107601 (2008).
- [27] A. B. Harris and T. Yildirim, Charge and spin ordering in the mixed-valence compound LuFe_2O_4 , *Phys. Rev. B* **81**, 134417 (2010).
- [28] F. Wang, J. Kim, G. D. Gu, Y. Lee, S. Bae, and Y.-J. Kim, Oxygen stoichiometry and magnetic properties of $\text{LuFe}_2\text{O}_{4+\delta}$, *J. Appl. Phys.* **113**, 063909 (2013).
- [29] M. Angst, R. P. Hermann, A. D. Christianson, M. D. Lumsden, C. Lee, M.-H. Whangbo, J.-W. Kim, P. J. Ryan, S. E. Nagler, W. Tian *et al.*, Charge Order in LuFe_2O_4 : Antiferroelectric Ground State and Coupling to Magnetism, *Phys. Rev. Lett.* **101**, 227601 (2008).
- [30] D. Niermann, F. Waschkowski, J. de Groot, M. Angst, and J. Hemberger, Dielectric Properties of Charge-Ordered LuFe_2O_4 Revisited: The Apparent Influence of Contacts, *Phys. Rev. Lett.* **109**, 016405 (2012).
- [31] J. de Groot, T. Mueller, R. A. Rosenberg, D. J. Keavney, Z. Islam, J.-W. Kim, and M. Angst, Charge Order in LuFe_2O_4 : An Unlikely Route to Ferroelectricity, *Phys. Rev. Lett.* **108**, 187601 (2012).
- [32] S. Lafuerza, J. García, G. Subías, J. Blasco, K. Conder, and E. Pomjakushina, Intrinsic electrical properties of LuFe_2O_4 , *Phys. Rev. B* **88**, 085130 (2013).
- [33] A. Kirilyuk, A. V. Kimel, and T. Rasing, Ultrafast optical manipulation of magnetic order, *Rev. Mod. Phys.* **82**, 2731 (2010).
- [34] N. Berggaard, V. Lopez-Flores, V. Halté, M. Hehn, C. Stamm, N. Pontius, E. Beaurepaire and C. Boeglin, Ultrafast angular momentum transfer in multisublattice ferrimagnets, *Nat. Commun.* **5**, 3466 (2014).
- [35] J. Becker, A. Tsukamoto, A. Kirilyuk, J. C. Maan, Th. Rasing, P. C. M. Christianen, and A. V. Kimel, Ultrafast Magnetism of a Ferrimagnet across the Spin-Flop Transition in High Magnetic Fields, *Phys. Rev. Lett.* **118**, 117203 (2017).
- [36] C. Kim, S. Lee, H.-G. Kim, J.-H. Park, K.-W. Moon, J. Y. Park, J. M. Yuk, K.-J. Lee, B.-G. Park, S. K. Kim *et al.*, Distinct handedness of spin wave across the compensation temperatures of ferrimagnets, *Nat. Mater.* **19**, 980 (2020).
- [37] M. Huang, M. U. Hasan, K. Klyukin, D. Zhang, D. Lyu, P. Gargiani, M. Valvidares, S. Sheffels, A. Churikova, F. Büttner *et al.*, Voltage control of ferrimagnetic order and voltage-assisted writing of ferrimagnetic spin textures, *Nat. Nanotechnol.* **16**, 981 (2021).
- [38] D. Afanasiev, J. R. Hortensius, B. A. Ivanov, A. Sasaki, E. Bousquet, Y. M. Blanter, R. V. Mikhaylovskiy, A. V. Kimel, and A. D. Caviglia, Ultrafast control of magnetic interactions via light-driven phonons, *Nat. Mater.* **20**, 607 (2021).
- [39] I. V. Anisimov, F. Aryasetiawan, and A. I. Lichtenstein, First-principles calculations of the electronic structure and spectra of strongly correlated systems: The LDA + U method, *J. Phys.: Condens. Matter* **9**, 767 (1997).
- [40] J. P. Perdew, K. Burke, and M. Ernzerhof, Generalized Gradient Approximation Made Simple, *Phys. Rev. Lett.* **77**, 3865 (1996).
- [41] G. Kresse and J. Hafner, *Ab initio* molecular dynamics for liquid metals, *Phys. Rev. B* **47**, 558(R) (1993).
- [42] G. Kresse and J. Furthmüller, Efficient iterative schemes for *ab initio* total-energy calculations using a plane-wave basis set, *Phys. Rev. B* **54**, 11169 (1996).
- [43] S. Fan, H. Das, A. Rébola, K. A. Smith, J. Mundy, C. Brooks, M. E. Holtz, D. A. Muller, C. J. Fennie, R. Ramesh *et al.*, Site-specific spectroscopic measurement of spin and charge in $(\text{LuFeO}_3)_m/(\text{LuFe}_2\text{O}_4)_1$ multiferroic superlattices, *Nat. Commun.* **11**, 5582 (2020).
- [44] R. D. King-Smith and David Vanderbilt, First-principles investigation of ferroelectricity in perovskite compounds, *Phys. Rev. B* **49**, 5828 (1994).

- [45] G. Henkelman, B. P. Uberuaga, and H. Jónsson, A climbing image nudged elastic band method for finding saddle points and minimum energy paths, *J. Chem. Phys.* **113**, 9901 (2000).
- [46] A. Zunger, S.-H. Wei, L. G. Ferreira, and J. E. Bernard, Special Quasirandom Structures, *Phys. Rev. Lett.* **65**, 353 (1990).
- [47] A. van de Walle, M. Asta, and G. Ceder, The alloy theoretic automated toolkit: A user guide, *Calphad* **26**, 539 (2002).
- [48] Z. Jiang, Y. Nahas, B. Xu, S. Prosandeev, D. Wang, and L. Bellaiche, Special quasirandom structures for perovskite solid solutions, *J. Phys.: Condens. Matter* **28**, 475901 (2016).
- [49] M. Shaikh, A. Fathima, M. J. Swamynadhan, H. Das, and S. Ghosh, Investigation into cation-ordered magnetic polar double perovskite oxides, *Chem. Mater.* **33**, 1594 (2021).
- [50] K. Lee, K. Shigematsu, H. Das, and M. Azuma, Exploring the correlation between the spin-state configuration and the magnetic order in Co-substituted BiFeO₃, *Phys. Rev. Mater.* **6**, 064401 (2022).
- [51] S. Steiner, S. Khmelevskiy, M. Marsman, and G. Kresse, Calculation of the magnetic anisotropy with projected-augmented-wave methodology and the case study of disordered Fe_{1-x}Co_x alloys, *Phys. Rev. B* **93**, 224425 (2016).
- [52] N. Metropolis and S. Ulam, The Monte Carlo method, *J. Am. Stat. Assoc.* **44**, 335 (1949).
- [53] N. Metropolis, A. W. Rosenbluth, M. N. Rosenbluth, and A. H. Teller, Equation of state calculations by fast computing machines, *J. Chem. Phys.* **21**, 1087 (1953).
- [54] N. A. Spaldin, Multiferroics: From the cosmically large to the subatomically small, *Nat. Rev. Mater.* **2**, 17017 (2017).
- [55] M. Fiebig, Th. Lottermoser, D. Fröhlich, A. V. Goltsev, and R. V. Pisarev, Observation of coupled magnetic and electric domains, *Nature (London)* **419**, 818 (2002).
- [56] T. Choi, Y. Horibe, H. T. Yi, Y. J. Choi, W. Wu, and S.-W. Cheong, Insulating interlocked ferroelectric and structural antiphase domain walls in multiferroic YMnO₃, *Nat. Mater.* **9**, 253 (2010).
- [57] Y. Geng, N. Lee, Y. J. Choi, S.-W. Cheong, and W. Wu, Collective magnetism at multiferroic vortex domain walls, *Nano Lett.* **12**, 6055 (2012).
- [58] Y. Kumagai and N. A. Spaldin, Structural domain walls in polar hexagonal manganites, *Nat. Commun.* **4**, 1540 (2013).
- [59] M. Lilienblum, T. Lottermoser, S. Manz, S. M. Selbach, A. Cano, and M. Fiebig, Ferroelectricity in the multiferroic hexagonal manganites, *Nat. Phys.* **11**, 1070 (2015).
- [60] M. Giraldo, Q. N. Meier, A. Bortis, D. Nowak, N. A. Spaldin, M. Fiebig, M. C. Weber, and T. Lottermoser, Magnetoelectric coupling of domains, domain walls and vortices in a multiferroic with independent magnetic and electric order, *Nat. Commun.* **12**, 3093 (2021).
- [61] M. E. Holtz, E. S. Padgett, R. Steinhardt, C. M. Brooks, D. Meier, D. G. Schlom, D. A. Muller, and J. A. Mundy, Dimensionality-Induced Change in Topological Order in Multiferroic Oxide Superlattices, *Phys. Rev. Lett.* **126**, 157601 (2021).
- [62] See Supplemental Material at <http://link.aps.org/supplemental/10.1103/PhysRevResearch.5.013007> for (i) additional results and discussions on the improper ferroelectric phases of the parent and carrier-doped LuFeO₃ systems (Figs. S1–S7), (ii) detailed description of the spin model, (iii) additional information about the Monte Carlo (MC) simulations and discussion on the results of MC calculations (Figs. S8–S21 and Tables S1 and S2), and (iv) discussions on the identified ferrimagnetic phases.
- [63] B. S. Holinsworth, D. Mazumdar, C. M. Brooks, J. A. Mundy, H. Das, J. G. Cherian, S. A. McGill, C. J. Fennie, D. G. Schlom, and J. L. Musfeldt, Direct band gaps in multiferroic *h* – LuFeO₃, *Appl. Phys. Lett.* **106**, 082902 (2015).
- [64] J. Zhang, P. V. Lukashev, S. S. Jaswal, and E. Y. Tsymlal, Model of orbital populations for voltage-controlled magnetic anisotropy in transition-metal thin films, *Phys. Rev. B* **96**, 014435 (2017).
- [65] S. Li and T. Birol, Free-Carrier-Induced Ferroelectricity in Layered Perovskites, *Phys. Rev. Lett.* **127**, 087601 (2021).
- [66] H. J. Xiang and M.-H. Whangbo, Charge Order and the Origin of Giant Magnetocapacitance in LuFe₂O₄, *Phys. Rev. Lett.* **98**, 246403 (2007).
- [67] W. Wu, V. Kiryukhin, H.-J. Noh, K.-T. Ko, J.-H. Park, W. Ratcliff, II P. A. Sharma, N. Harrison, Y. J. Choi, Y. Horibe *et al.*, Formation of Pancakelike Ising Domains and Giant Magnetic Coercivity in Ferrimagnetic LuFe₂O₄, *Phys. Rev. Lett.* **101**, 137203 (2008).
- [68] K.-T. Ko, H.-J. Noh, J.-Y. Kim, B.-G. Park, J.-H. Park, A. Tanaka, S. B. Kim, C. L. Zhang, and S.-W. Cheong, Electronic Origin of Giant Magnetic Anisotropy in Multiferroic LuFe₂O₄, *Phys. Rev. Lett.* **103**, 207202 (2009).
- [69] F. Wang, J. Kim, Y.-J. Kim, and G. D. Gu, Spin-glass behavior in LuFe₂O_{4+δ}, *Phys. Rev. B* **80**, 024419 (2009).
- [70] V. Kataev, A. Möller, U. Löw, W. Jung, N. Schittner, M. Kriener, and A. Freimuth, Structural and magnetic properties of the new low-dimensional spin magnet InCu_{2/3}V_{1/3}O₃, *J. Magn. Magn. Mater.* **290-291**, 310 (2005).
- [71] Y. Yan, Z. Li, T. Zhang, X. Luo, G. Ye, Z. Xiang, P. Cheng, L.-J. Zou, and X. Chen, Magnetic properties of the doped spin- $\frac{1}{2}$ honeycomb-lattice compound In₃Cu₂VO₉, *Phys. Rev. B* **85**, 085102 (2012).
- [72] A. Jain, S. P. Ong, G. Hautier, W. Chen, W. D. Richards, S. Dacek, S. Cholia, D. Gunter, D. Skinner, G. Ceder, and K. Persson, Commentary: The Materials Project: A materials genome approach to accelerating materials innovation, *APL Mater.* **1**, 011002 (2013).
- [73] X. Pan, A. Zhang, J. Zhu, and X. Wu, Structural, electrical, and magnetic properties of hexagonal Lu_{0.5-x}Zr_xSc_{0.5}FeO₃ ceramics, *Phys. Status Solidi B*, 2200400 (2022).
- [74] J. Nordlander, M. A. Anderson, C. M. Brooks, M. E. Holtz, and J. A. Mundy, Epitaxy of hexagonal ABO₃ quantum materials, *Appl. Phys. Rev.* **9**, 031309 (2022).
- [75] S. M. Disseler, X. Luo, B. Gao, Y. Seok Oh, R. Hu, Y. Wang, D. Quintana, A. Zhang, Q. Huang, J. Lau *et al.*, Multiferroicity in doped hexagonal LuFeO₃, *Phys. Rev. B* **92**, 054435 (2015).
- [76] K. A. Smith, S. P. Ramkumar, N. C. Harms, A. J. Clune, S.-W. Cheong, Z. Liu, E. A. Nowadnick, and J. L. Musfeldt, Pressure-induced phase transition and phonon softening in *h* – Lu_{0.6}Sc_{0.4}FeO₃, *Phys. Rev. B* **104**, 094109 (2021).
- [77] Y. K. Jeong, J.-H. Lee, S.-J. Ahn, and H. M. Jang, Epitaxially constrained hexagonal ferroelectricity and canted triangular spin order in LuFeO₃ thin films, *Chem. Mater.* **24**, 2426 (2012).
- [78] H. Iida, T. Koizumi, Y. Uesu, K. Kohn, N. Ikeda, S. Mori, R. Haumont, P.-E. Janolin, J.-M. Kiat, M. Fukunaga, and Y. Noda,

- Ferroelectricity and ferrimagnetism of hexagonal YbFeO_3 thin films, *J. Phys. Soc. Jpn.* **81**, 024719 (2012).
- [79] S.-J. Ahn, J.-H. Lee, H. M. Jang, and Y. K. Jeong, Multiferroism in hexagonally stabilized TmFeO_3 thin films below 120 K, *J. Mater. Chem. C* **2**, 4521 (2014).
- [80] Y. Hamasaki, T. Shiraishi, T. Taniyama, T. Katayama, S. Yasui, A. Akama, T. Kiguchi, and M. Itoh, Switchable third ScFeO_3 polar ferromagnet with YMnO_3 -type structure, *J. Mater. Chem. C* **8**, 4447 (2020).
- [81] B. Chen, H. Ohta, and T. Katayama, Ferroelectric and magnetic properties of hexagonal ErFeO_3 epitaxial films, *ACS Appl. Electron. Mater.* **4**, 4547 (2022).
- [82] K. Rogdakis, J. W. Seo, Z. Viskadourakis, Y. Wang, L. F. N. Ah Qune, E. Choi, J. D. Burton, E. Y. Tsybmal, J. Lee, and C. Panagopoulos, Tunable ferroelectricity in artificial tri-layer superlattices comprised of non-ferroic components, *Nat. Commun.* **3**, 1064 (2012).
- [83] M. P. Warusawithana, C. S. Kengle, X. Zhan, H. Chen, E. V. Colla, M. O’Keeffe, J.-M. Zuo, M. B. Weissman, and J. N. Eckstein, Asymmetric ferroelectricity by design in atomic-layer superlattices with broken inversion symmetry, *Phys. Rev. B* **104**, 085103 (2021).
- [84] J. Hong and D. Vanderbilt, Mapping the energy surface of PbTiO_3 in multidimensional electric-displacement space, *Phys. Rev. B* **84**, 115107 (2011).
- [85] J. T. Heron, J. L. Bosse, Q. He, Y. Gao, M. Trassin, L. Ye, J. D. Clarkson, C. Wang, Jian Liu, S. Salahuddin *et al.*, Deterministic switching of ferromagnetism at room temperature using an electric field, *Nature (London)* **516**, 370 (2014).